Energy & Environmental Science

RSC Publishing

PAPER

View Article Online
View Journal | View Issue

Cite this: *Energy Environ. Sci.*, 2013, **6**, 3007

Visible-light photocatalytic, solar thermal and photoelectrochemical properties of aluminium-reduced black titania†

Zhou Wang,[ab] Chongyin Yang,[ab] Tianquan Lin,[ab] Hao Yin,[a] Ping Chen,[a] Dongyun Wan,[a] Fangfang Xu,[a] Fuqiang Huang,*[ab] Jianhua Lin,[b] Xiaoming Xie[c] and Mianheng Jiang[c]

Received 27th May 2013
Accepted 15th July 2013

DOI: 10.1039/c3ee41817k

www.rsc.org/ees

Utilizing solar energy for hydrogen generation and water cleaning is a great challenge due to insufficient visible-light power conversion. Here we report a mass production approach to synthesize black titania by aluminium reduction. The obtained sample possesses a unique crystalline core–amorphous shell structure (TiO_2@TiO_{2-x}). The black titania absorbs ~65% of the total solar energy by improving visible and infrared absorption, superior to the recently reported ones (~30%) and pristine TiO_2 (~5%). The unique core–shell structure (TiO_2@TiO_{2-x}) and high absorption boost the photocatalytic water cleaning and water splitting. The black titania is also an excellent photoelectrochemical electrode exhibiting a high solar-to-hydrogen efficiency (1.7%). A large photothermic effect may enable black titania "capture" solar energy for solar thermal collectors. The Al-reduced amorphous shell is proved to be an excellent candidate to absorb more solar light and receive more efficient photocatalysis.

Introduction

Titanium dioxide (TiO_2) as an important semiconductor has attracted extensive interest in the fields of photocatalysis, solar cells and solar thermal collectors (*i.e.*, blue titania), although the wide-band-gap material (~3.2 eV) captures about 5% of solar energy.[1–6] Many investigations have been attempted to enhance visible-light absorption by band structure engineering (*e.g.* element doping and oxygen deficiency).[7–12] Nevertheless, the visible-light power harvest remains insufficient due to little effective light absorption and many carrier-recombination centers.[13] Very recently, the hydrogenation of black titania can boost its visible and infrared light absorption and ultraviolet (UV) light photocatalytic activity.[14–18] The improved solar absorption is attributed to additional intermediate electronic states induced by hydrogen insertion into the lattice of TiO_2.[15] However, this absorption enhancement is not very effective for visible-light photocatalysis.[9,19–21]

Recently, black TiO_2 has attracted enormous attention.[14–16,19,20,22–26] There are two major preparation methods: (i) high H_2-pressure process and (ii) hydrogen gas annealing. The first one is good for photocatalysis but the synthesis is troublesome as in a high-pressure hydrogen atmosphere (20 bar) for five days.[15] The second one starting from amorphous TiO_2 cannot ensure good photocatalytic activity. Therefore, a facile synthesis is demanded to produce black titania with large solar absorption and excellent photocatalytic activity.

The rapid aluminothermic reduction reaction of TiO_2 and elemental aluminum (Al) was used over 50 years ago to produce Al–Ti alloy.[27] Inspired by this old technique, a controllable low-temperature synthetic route for black TiO_{2-x} was developed using melted Al as a reductant in an evacuated two-zone vacuum furnace. The Al decreases oxygen partial pressure to provide a kinetic driving force to efficiently reduce TiO_2 at a lower temperature (300–500 °C). This method is suitable for the mass production of black TiO_2. This black titania has a unique crystalline core–amorphous shell structure (TiO_2@TiO_{2-x}). Improved visible and infrared light absorption boosts photocatalysis on both water splitting and waste-water cleaning and enables black titania "capture" solar energy for solar thermal collectors. Furthermore, this oxygen-deficient black titania achieves a rather high solar-to-hydrogen efficiency, which can be applied as an excellent photoelectrochemical electrode.

[a]*CAS Key Laboratory of Materials for Energy Conversion, Shanghai Institute of Ceramics, Chinese Academy of Sciences, Shanghai 200050, China. E-mail: huangfq@mail.sic.ac.cn*

[b]*Beijing National Laboratory for Molecular Sciences, College of Chemi stry and Molecular Engineering, Peking University, Beijing 100871, China*

[c]*State Key Laboratory of Functional Materials for Informatics, Shanghai Institute of Microsystem and Information Technology, Chinese Academy of Sciences, Shanghai 200050, China*

† Electronic supplementary information (ESI) available. See DOI: 10.1039/c3ee41817k

Experimental section

Preparation of black TiO_{2-x}

TiO_2 samples and aluminum were placed separately in a two-zone tube furnace (Fig. S1a†) and then evacuated to a base pressure lower than 0.5 Pa, and the detailed discussion is provided in the ESI.† After that, aluminum was heated at 800 °C, and TiO_2 samples were heated at 300 °C, 400 °C, 500 °C, and 600 °C for 6 h and 20 h, respectively. The post-annealing treatment was conducted by heating the 500 °C-Al–TiO_{2-x} sample at 800 °C and 900 °C in an Ar atmosphere for 12 h, respectively.

Preparation of H_2–TiO_{2-x}

TiO_2 samples were placed in a tube furnace and then evacuated to a base pressure of about 0.5 Pa. After that, TiO_2 samples were heated at 500 °C for 6 h in H_2 flow under atmospheric pressure.

UV light photocatalytic degradation

The UV light photocatalytic activity of the TiO_2 sample was evaluated by monitoring the decomposition of methyl orange in an aqueous solution under UV irradiation from a 300 W Hg lamp. A Pyrex glass vessel was used as the photoreactor. The TiO_2 sample (100 mg) was mixed with methyl orange solution (100 mL, 0.1 M). After stirring for 30 min in the dark to reach the adsorption equilibrium, the solution was illuminated with a 300 W Hg lamp. The solution was cooled by the water circulating jacket of the reactor to avoid the interference of the solvent evaporation. The concentration of aqueous methyl orange was determined with a UV-Vis spectrophotometer by measuring the peak intensity at 464 nm.

Visible light photocatalytic degradation

The visible light photocatalytic activity of the TiO_2 sample was evaluated by monitoring the decomposition of phenol and methyl orange in an aqueous solution under AM 1.5G simulated solar light cut off by a 400 nm filter. The emission spectrum of the simulator is illustrated in Fig. S2.† A Pyrex glass vessel was used as the photoreactor. For the degradation of MO, 100 mg of TiO_2 sample was added to 100 mL MO solution with a concentration of 0.1 M. For the degradation of phenol, the concentration of the solution was changed to 0.3 M. After stirring for 30 min in the dark to reach the adsorption equilibrium, the solution was illuminated with the solar simulator. The solution was cooled by the water circulating jacket of the reactor to avoid the interference of the solvent evaporation. The concentration of aqueous phenol was determined with a UV-Vis spectrophotometer by measuring the peak intensity at 270 nm.

Photocatalytic H_2 generation

100 mg of photocatalyst loaded with 0.5 wt% Pt was added to an aqueous methanol solution (120 mL, 25%) in a closed gas circulation system. The UV light and visible light irradiation were obtained from a 300 W Hg lamp and an AM 1.5G solar light simulator cut off by a 400 nm filter, respectively. Methanol was used as a sacrificial reagent, and the anodic reaction generating O_2 from H_2O did not occur. The amount of H_2 generated was determined by gas chromatography.

Photoelectrochemical cell (PEC)

PEC measurements were performed in a typical three-electrode potentiostat system (Parstat 2773), in which the TiO_2 film on a FTO substrate, a Pt wire, and an Ag/AgCl electrode were used as the working, counter, and reference electrodes, respectively. 1.0 M NaOH aqueous solution was used as the supporting electrolyte to maintain the stability of films. A solar simulator (AM 1.5) with a power of 100 mW cm^{-2} was used as the illumination source. Photocurrent ON/OFF cycles were measured using the same electrochemical workstation coupled with a mechanical chopper.

Results and discussion

Structure features and physical properties

A similar morphology and particle size of the TiO_2 nanocrystals before and after the Al reduction were verified by transmission electron microscopy (TEM). These nanocrystals are averagely ~25 nm in diameter, as shown in Fig. 1a and b. The pristine TiO_2 nanocrystals are highly crystallized, as the well-resolved lattice features are shown in the high-resolution TEM (HRTEM)

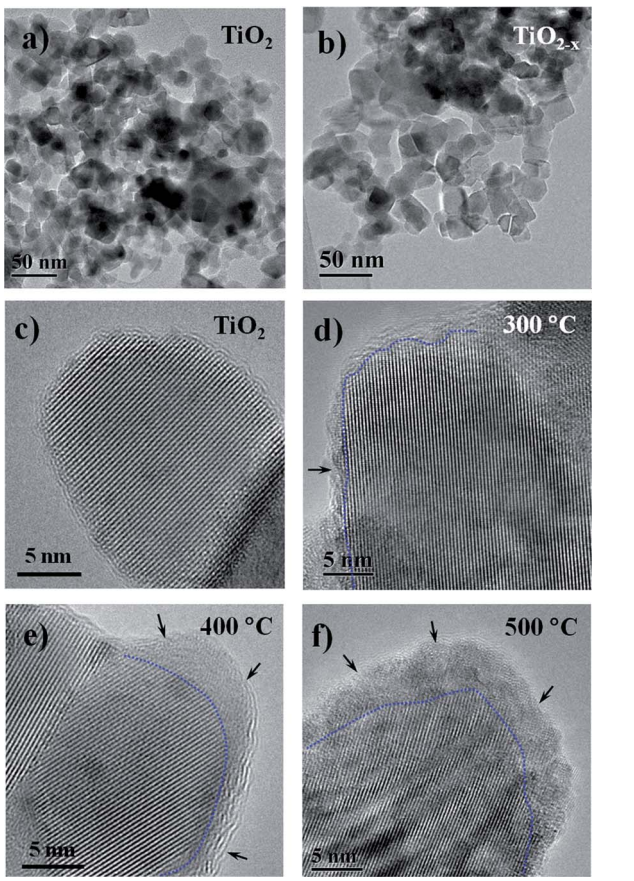

Fig. 1 TEM images of titania nanocrystals before (a: TiO_2) and after (b: TiO_{2-x}) reduction; (c–f) HRTEM images of TiO_2 nanocrystals before (c) and after (d–f) the Al reduction at different temperatures for 6 h.

image (Fig. 1c). The 6 h-300 °C-Al-reduced nanocrystals display a unique core–shell structure of TiO_2@TiO_{2-x} (~1.5 nm thick disordered surface layer (TiO_{2-x}) coating on a crystalline core of TiO_2). The thickness of the disordered layer increases with the Al-reduction temperature in the temperature interval of 300–500 °C, as shown in Fig. 1d and e. (The core–shell TiO_2@TiO_{2-x} sample is denoted as TiO_{2-x} from now on for simplification.) When prolonging the Al-reduction time to 20 h at 500 °C, the nanocrystals reveal more imperfections and mostly lose the core–shell structure (Fig. S3†); when increasing the reduction temperature to 600 °C for 6 h, the nanocrystals are highly crystalline without any shells (Fig. S4†).

As illustrated in Fig. 2a, a large amount of black TiO_{2-x} was achieved from one batch by our Al-reduction route. The Al-reduced TiO_{2-x} samples extend the photoresponse from ultraviolet (UV) light to visible and infrared light regions, as shown in Fig. 2b. All these samples possess a band gap value (E_g ~ 3.2 eV), similar to pristine TiO_2, and an add-on absorption shoulder peak at ~500 nm is imposed onto the cutoff edge. Significantly enhanced absorption occurs from ~400 nm to the near-infrared region. As mentioned above, the H_2 molecule cannot efficiently reduce TiO_2 at low temperature (*i.e.* 500 °C), as confirmed by the HRTEM image shown in Fig. S5.† The wide-spectrum absorption in TiO_{2-x} increases with the reduction temperature (Fig. 2b), which may be correlated with the amount of Ti^{3+} in the shell. In order to verify the heterogeneous core–shell structure of TiO_{2-x}, the 500 °C-Al-reduced TiO_{2-x} was annealed at 800 °C and 900 °C (Fig. S6†) for 12 h in an Ar atmosphere, respectively. The color of the samples turned from black to gray (800 °C) to white (900 °C) (Fig. S7†) and the light absorption decreased obviously (Fig. S8†). It is presumably due to that the Ti^{3+} atoms/oxygen vacancies diffuse from shell to core, and the defects as "*color centers*" are also diluted. The HRTEM image of the 900 °C-annealed sample reveals that the amorphous shell of nanocrystals vanishes after annealing, as shown in Fig. S5b.†

The oxygen deficiency and amorphous surface of TiO_{2-x} are unambiguously supported by Raman spectroscopy, as six characteristic Raman bands of TiO_2 are shown in Fig. 3a. For three black TiO_{2-x} nanocrystals, the strongest E_g mode area at 144 cm^{-1} amplifies and exhibits a blue shift accompanied by peak broadening, compared with pristine TiO_2. As reported in the previous studies,[28,29] the shift and broadening of the peaks of TiO_2 were ascribed to the crystal domain size and non-stoichiometry. Similar BET specific surface areas for these black TiO_{2-x} (~42 m^2 g^{-1}) and pristine TiO_2 (~43 m^2 g^{-1}) confirm that the crystal size of black TiO_{2-x} does not increase after the Al reduction, consistent with the observations of the TEM results discussed above. Thus, the blue shift of the strongest mode at 144 cm^{-1} and broader linewidth can be attributed to the oxygen vacancies existing in the black TiO_{2-x} (nonstoichiometric). As the X-ray power diffraction (XRD) patterns illustrated in Fig. S9,† the strong diffraction peaks indicate that pristine TiO_2 (P25, a mixture of anatase and rutile) and black TiO_{2-x} remain highly crystalline. Nevertheless, the black TiO_{2-x} exhibits a larger linewidth than pristine TiO_2, which is derived from oxygen vacancies, as-resulted disorder-induced lattice strains and slightly reduced crystal size.

The plots of magnetic field dependence of magnetization are shown in Fig. 3b. The reduction degree (x) of TiO_{2-x} can be indexed *via* the magnetic field dependence of the magnetization

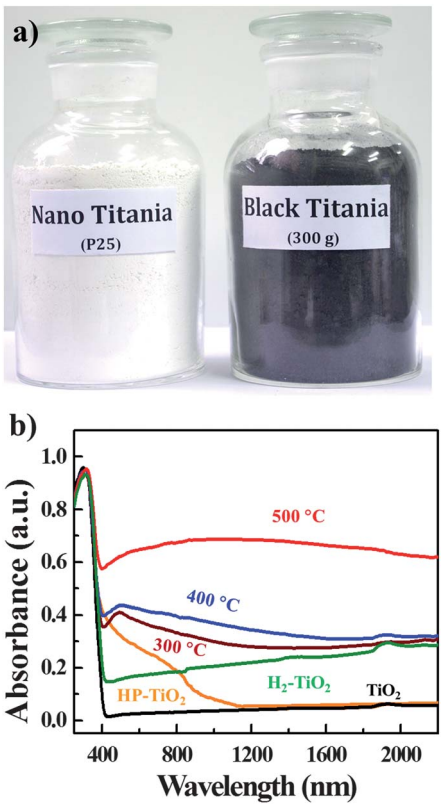

Fig. 2 (a) Mass production of black titania (TiO_{2-x}) using our Al-reduction method. (b) Absorption spectra of TiO_{2-x} samples reduced at different temperatures (300 °C, 400 °C, and 500 °C), the high-pressure hydrogenated black titania (HP-TiO_2, from ref. 15), the H_2-reduced titania (H_2–TiO_{2-x}), and pristine titania (TiO_2).

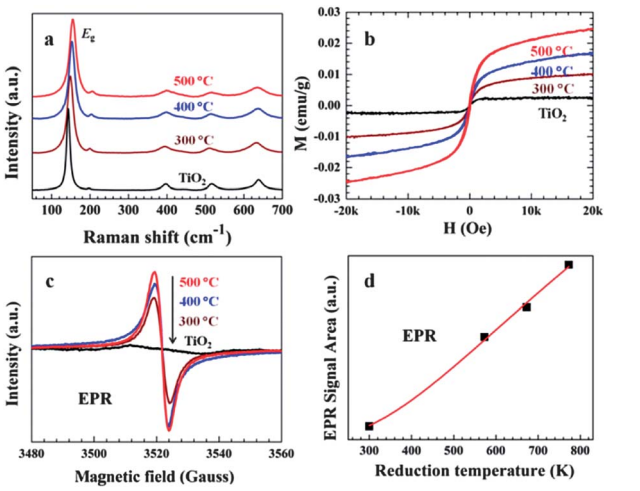

Fig. 3 (a) Raman spectra, (b) magnetic field dependence of magnetization and (c) EPR spectra of black TiO_{2-x} and pristine TiO_2 as a reference sample. (d) Correlation of the signal area obtained from double integration of the Ti^{3+} signal to the Al-reduction temperature.

recorded at 300 K. As an efficacious probe, the field dependence of magnetization indicates that the localized Ti^{3+} spins play a crucial role in introducing ferromagnetism into TiO_2. It is evident that ferromagnetic and paramagnetic moments coexist in all TiO_{2-x} samples, consistent with the reported oxygen-deficient TiO_{2-x}.[30,31] When increasing the Al reduction temperature, the sample has stronger magnetization, as shown in the figure, which may be partially correlated with the higher concentration of Ti^{3+}. The saturation magnetization M_s for samples reckoned from the partial hysteresis loops is 0.010 emu g^{-1} for the 300 °C-reduced sample, 0.017 emu g^{-1} for 400 °C and 0.025 emu g^{-1} for 500 °C, respectively. The Ti^{3+} states in the TiO_{2-x} samples were also investigated by electron paramagnetic resonance (EPR). A strong EPR signal observed at $g = 2.002$ is assigned to Ti^{3+} (Fig. 3c).[32] The signal area is correlated with the amount of Ti^{3+}, and a nearly linear correlation

$$n = n_0 \exp(-\Delta E/kT),$$

(where n is the molar content of Ti^{3+}, n_0 is a fitting coefficient, ΔE is the escape energy of O atoms in Al-reduction, and T is the temperature) between the EPR signal area and the Al-reduction temperature is found, as shown in Fig. 3d. A large amount of Ti^{3+} (V_O) may exist in the TiO_{2-x} samples.

X-ray photoelectron spectroscopy (XPS) can provide useful information of chemical binding and valence band position on the sample surface as shown in Fig. 4. Unexpectedly, the spectra of Ti 2p XPS, O 1s XPS and valence band are almost identical for both pristine TiO_2 and TiO_{2-x}, which were similarly found in some reported black titania.[14] The Ti $2p_{3/2}$ and $2p_{1/2}$ XPS peaks centered at binding energies of 458.5 and 464.3 eV are typical for the Ti^{4+}–O bonds in TiO_2. The single O 1s XPS peak at 529.8 eV for TiO_2 can be also assigned to Ti–O bonds. The valence band maxima are estimated by linear extrapolation of the peaks to the baselines, which derives a band edge position of 2.05 eV below the Fermi energy.[33] No peak shifts and no additional peaks of Ti^{3+} found in our TiO_{2-x} sample might be subjected to the detection distance (~ten atomic layers) for XPS. More possibly, surface metastable sites (surfaced Ti^{3+} atoms, oxygen vacancies) in loosely packed amorphous shells were easily oxidized by certain components (O_2, H_2O, *etc.*) in air. Moreover, no aluminum was detected in the full XPS spectrum (Fig. S10†).

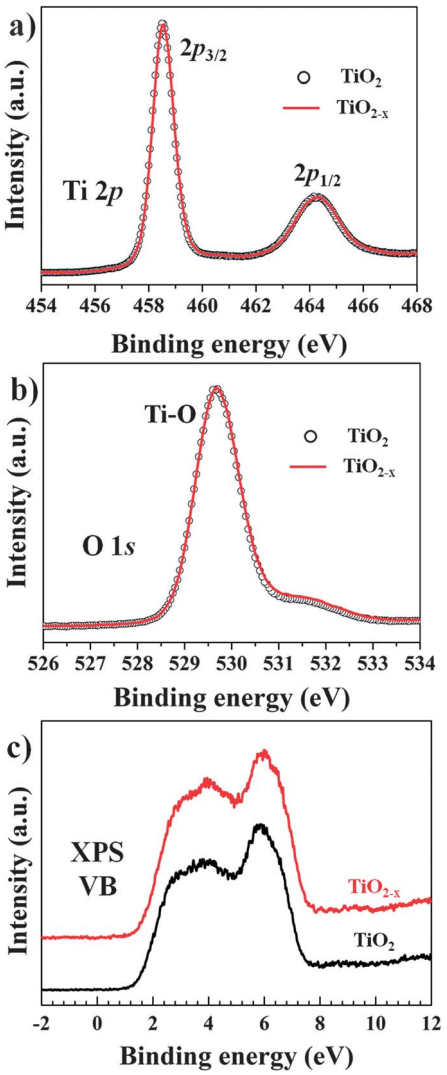

Fig. 4 (a) Ti 2p XPS spectra, (b) normalized O 1s XPS spectra and (c) XPS valence band spectra of pristine TiO_2 and TiO_{2-x}.

Solar thermal effect

Compared with the solar spectrum shown in Fig. 5a, the Al-reduced TiO_{2-x} samples extend the absorption from ultraviolet (UV) light to visible and infrared light regions. Compared with pristine TiO_2 (P25) with little absorption in visible and infrared light regions, the total solar absorption of the 500 °C-reduced TiO_{2-x} sample reaches about 65%. In contrast, the high-pressure hydrogenated black titania (HP–TiO_2, data from ref. 15) has a little absorption in the infrared light region (1%) and its total solar absorption is about 30%, as shown in Table S1.† The enhanced solar absorption of black titania was further investigated from the photothermic effect by the irradiation of an AM 1.5G Xe lamp solar simulator. The investigated disks were cold-pressed from TiO_2 and 500 °C-reduced TiO_{2-x} powders. As illustrated in Fig. 5b, after being irradiated for 60 s, the temperature of the black TiO_{2-x} disk increased to 37 °C, compared to 28 °C for the pristine TiO_2 disk. The accelerated heating rate of the black TiO_{2-x} disk is attributed to larger solar absorption demonstrated by the absorption spectrum in Fig. 5a, resulting in more electron excitation and relaxation and intensified heat emission. Potentially, our black titania can be applied as a solar absorber material for solar thermal collection.

Photocatalytic dye degradation and hydrogen generation

The photocatalytic activities of the TiO_{2-x} samples were evaluated by the decomposition of methyl orange (MO) under UV light irradiation, as shown in Fig. 6. The photocatalytic activity of the TiO_{2-x} samples increased with the Al reduction temperature, which is consistent with the trend of the enhancement of solar absorption. For the 500 °C-reduced TiO_{2-x}, the photodegradation was completed after 12 min, whereas pristine TiO_2 had more than 17% residual of MO. The 500 °C-reduced TiO_{2-x}

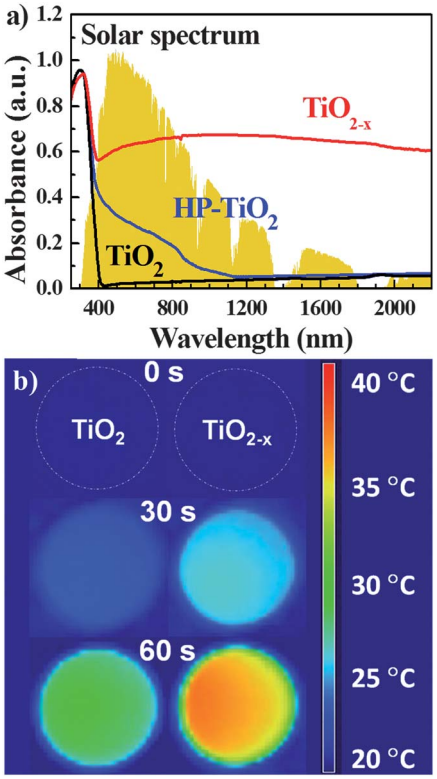

Fig. 5 (a) Absorption spectra of the 500 °C-reduced TiO_{2-x} sample, the high-pressure hydrogenated black titania (HP–TiO_2, from ref. 15), and pristine titania (TiO_2). (b) Thermal image map of cool-pressed disks (from TiO_2 and 500 °C-reduced TiO_{2-x} powders) after irradiation under an AM 1.5G Xe lamp solar simulator for different times.

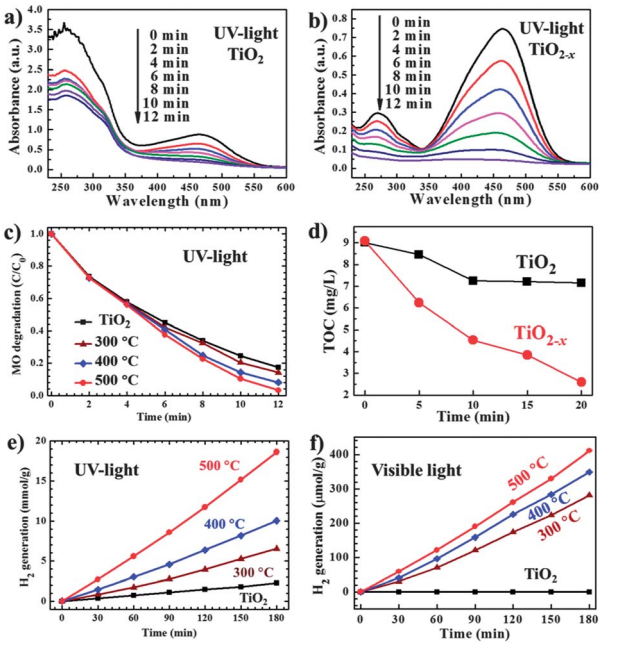

Fig. 6 Absorption spectra of methyl orange after UV light photocatalytic degradation with (a) pristine TiO_2 and (b) 500 °C-reduced black TiO_{2-x}. (c) UV light photocatalytic degradation of methylene orange. (d) Disappearance of total organic carbon (TOC) during the UV-light photocatalytic degradation of MO with 500 °C-reduced black TiO_{2-x} and pristine titania (TiO_2). H_2 generation of black TiO_{2-x} under (e) UV light and (f) visible light irradiation.

retained good photocatalytic activity in ten cycles, as shown in Fig. S11.† Surprisingly, it exhibited gradually accelerating degradation during the first three cycles, and the final stabilized MO degradation time was 10 min. It is evident that the EPR signal of Ti^{3+} is weakened when the 500 °C-reduced TiO_{2-x} was irradiated under the UV light in water for 30 min or after the first two cycles of photocatalytic degradation, as shown in Fig. S12.† The localized Ti^{3+} states and oxygen vacancies have been considered to be the recombination centers of light-induced electrons and holes.[4] During the UV irradiation, some Ti^{3+} sites on the surface are converted into Ti^{4+} and therefore these recombination centers are reduced, resulting in improved photocatalytic activity. This may also explain why the XPS cannot detect the existence of Ti^{3+}. Furthermore, the Ti^{3+} species in an amorphous shell–crystalline core structure are much easier to be oxidized to Ti^{4+} than those in the well-crystallized oxygen-deficient titania. The photocatalysis of the 600 °C-reduced sample is even poorer than that of TiO_2 (P25), as shown in Fig. S13.† It indicates that the amorphous shell–crystalline core structure is important to improve the photocatalysis.

The previous MO photocatalytic degradation is simply evaluated to monitor the absorption peak at 464 nm, which is assigned to the n → π* transition related to the azo bond under strong influence of the electron-donating dimethylamino group.[34,35] This evaluation only quantitatively indicates the initial step of degradation (breaking the N=N bonding), but the complete decomposition of MO also includes breaking down the benzene ring, decomposing to organic micromolecules, and finally being mineralized to inorganic ions (CO_3^{2-}, NO_3^-, and NH_4^+). As shown in Fig. 6a, the original MO possesses two characteristic peaks located at 273 nm and 464 nm, which are attributed to the π → π* transition located in the aromatic rings and the n → π* transition related to the azo bond, respectively.[34–36] When applying pristine titania as the catalyst, the absorption peak at 464 nm nearly vanished after 12 min. However, the intensity of the lower absorption peak at 273 nm decreased slowly, indicating the incomplete decomposition of MO. When using 500 °C-Al reduced TiO_{2-x}, MO was completely degraded for both peaks after 12 min, suggesting the high mineralization efficiency. Obviously, our Al-reduced TiO_{2-x} decomposes MO faster and more completely. Total organic carbon (TOC) measurements (Fig. 6d) were conducted to further confirm the efficient mineralization of organic carbon of the photodegradation of MO by 500 °C-Al reduced TiO_{2-x}. Only 26% of TOC still remained in the suspension after 20 min irradiation when MO was completely transformed. The final mineralization yield reached a value of 74%. As a reference, pristine TiO_2 had more than 79% residual of TOC after 20 min, indicating that our black titania can degrade organic pollutants more completely.

Visible-light catalytic activity was further investigated to evaluate the visible-light photocatalysis of the TiO_{2-x} samples. As shown in Fig. S14,† the Al-reduced TiO_{2-x} samples exhibit

obviously improved photocatalytic activity. The 500 °C-Al-reduced TiO_{2-x} sample degraded 52% of MO after 6 h, whereas pristine TiO_2 degraded only 4% of MO. Phenol, which absorbs no visible light, was also applied as the decomposition substrate to avoid the interference from the absorption of dye. As shown in Fig. S15,† the 500 °C-Al-reduced TiO_{2-x} sample degraded 78% of the phenol after 3.5 h, but pristine TiO_2 had 82% residual of phenol.

The photocatalytic water splitting of the black TiO_{2-x} samples was further performed to produce hydrogen gas, as shown in Fig. 6e. The amount of H_2 generation increases with the Al-reduction temperature, similar to methyl orange degradation. The 500 °C-reduced sample steadily produced hydrogen gas at about 6.4 mmol h^{-1} g^{-1}, which is 8.5 times higher than that of pristine TiO_2 (0.75 mmol h^{-1} g^{-1}) and comparable to the reported excellent photocatalysts.[21,37] The visible-light photocatalysis of water splitting experiment is shown in Fig. 6f. The 500 °C-Al-reduced TiO_{2-x} sample steadily produced hydrogen gas at about 140 μmol h^{-1} g^{-1}, compared with no hydrogen detected for pristine TiO_2. These results have verified that the core–shell structure of TiO_{2-x} nanocrystals can enhance the photocatalytic activity.

Photoelectrochemical cell (PEC)

In order to further investigate the photoelectrochemical properties, pristine anatase TiO_2 films were prepared on FTO glass substrates by magnetron sputtering a TiO_2 target in an atmosphere of 5% O_2 + 95% Ar. The as-sputtered films were first annealed at 500 °C for 2 h in air and further aluminum-reduced at 500 °C for 4 h (Fig. S16†). The TiO_{2-x} layer was formed on the top of the TiO_2 film. A set of linear-sweep photovoltammograms were recorded in the dark and under illumination from an AM 1.5 solar spectrum simulator, as shown in Fig. 7a. The potential was swept linearly at a scan rate of 10 mV s^{-1} between 0.0 and 1.5 V_{RHE} in a 1 M NaOH electrolyte (PH = 13.6). Both photoelectrodes showed insignificant dark current (<10^{-4} mA cm^{-2}), indicating that no electrocatalytic oxygen evolution occurred. Under illumination, the TiO_{2-x} electrode had a significant increase in photocurrent density, which is three times as high as that of TiO_2 at 1.23 V_{RHE} (corresponding to the potential of the reversible oxygen electrode). Furthermore, the onset potential of the photocurrent revealed a drastic shift from 0.45 V_{RHE} for TiO_2 to 0.18 V_{RHE} for TiO_{2-x}. The higher photocurrent density and the lower onset potential demonstrate more efficient charge separation and transportation in the black TiO_{2-x} film, compared with the pristine TiO_2 film.

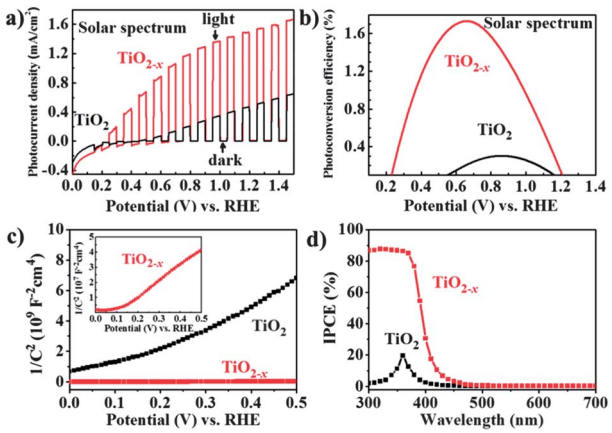

Fig. 7 Photoelectrochemical properties of pristine TiO_2 and Al-reduced black TiO_{2-x} electrodes: (a) chopped *J–V* curves under simulated solar light illumination using a three electrode setup (TiO_2 working, Pt counter, Ag/AgCl reference electrode, scan rate of 10 mV s^{-1}) in a 1 M NaOH electrolyte (pH = 13.6); (b) photoconversion efficiency as a function of applied potential; (c) Mott–Schottky plots collected at a frequency of 5 kHz in the dark; (d) IPCE spectra in the region of 300–700 nm at 0.65 V_{RHE}.

The solar-to-hydrogen (STH) efficiencies (η) of photoanodes were calculated using the equation

$$\eta = I(1.23 - V)/J_{light},$$

where V is the applied bias *vs.* RHE, I is the photocurrent density at the measured bias, and J_{light} is the irradiance intensity of 100 mW cm^{-2} (AM 1.5G). The calculated STH efficiency plotted as a function of the applied bias is shown in Fig. 7b. The pristine TiO_2 sample exhibited an optimal conversion efficiency of ~0.28% at 0.87 V_{RHE}. Significantly, the TiO_{2-x} sample achieved a very high efficiency at a lower bias of 0.65 V_{RHE} (~1.7%), which is among the best STH efficiencies (0.5–1.6%) for TiO_2-based photoanodes.[23,38] The PEC results imply that Al-reduction treatment substantially enhanced the photoconversion efficiency of TiO_2 by improving the maximum photocurrent and reducing the driving potential.

The electrochemical impedance measurements were conducted on the pristine TiO_2 and TiO_{2-x} samples, and both samples showed a positive slope in the Mott–Schottky plots, as expected for n-type semiconductors (Fig. 7c). The TiO_{2-x} sample showed a substantially smaller slope of the Mott–Schottky plot than the TiO_2 sample, suggesting an increase of donor density. The carrier density was calculated from the slope of Mott–Schottky plots using the following equation,

$$N_d = (2/e_0\varepsilon\varepsilon_0)[d(1/C^2)/dV]^{-1},$$

where e_0 is the electron charge, ε is the dielectric constant of TiO_2 ($\varepsilon = 170$), ε_0 is the permittivity of vacuum, N_d is the donor density, and V is the applied bias at the electrode. The calculated electron densities of TiO_2 and TiO_{2-x} were 7.67×10^{17} and 5.61×10^{19} cm^{-3}, respectively.

In order to understand the interplay between the photoactivity and the light absorption of TiO_2, incident-photon-to-current-conversion efficiency (IPCE) measurements were performed on pristine TiO_2 and Al-reduced black TiO_{2-x} photoanodes at 0.65 V_{RHE} (Fig. 7d). The IPCE can be expressed by the following equation

$$IPCE = (1240I)/(\lambda J_{light}),$$

where I is the measured photocurrent density at a specific wavelength, λ is the wavelength of incident light, and J_{light} is the measured irradiance at a specific wavelength. In comparison with pristine TiO_2, TiO_{2-x} exhibits greatly enhanced

photoactivity over the entire UV region and reached the IPCE values uniformly higher than 85% in the wavelength range from 300 to 370 nm. It indicates that the UV light was effectively used for PEC water splitting, in which the separation and transportation of photoexcited charge carriers are more efficient in TiO_{2-x}. The recognizable photoactivity was also observed in the visible light region for the TiO_{2-x} sample, whereas the IPCE value of TiO_{2-x} is higher than that of pristine TiO_2 in the visible light region from 400 nm to 470 nm. It indicates that Al-reduction not only highly enhances the efficiency of photoelectric conversion under UV light, but also extends the range of photoresponse into the visible-light region.

Electronic structure

The electronic structures of the core–shell structured TiO_2@TiO_{2-x} are shown in Fig. 8. The band structure contributed from the crystalline core is similar to the anatase TiO_2 phase, and the TiO_{2-x} shell mainly provides some dispersed Ti^{3+} 3d below CBM and O $2p^6$ above VBM. Therefore, the schematic electronic structures of TiO_2 and TiO_2@TiO_{2-x} (denoted as TiO_{2-x}) are proposed in Fig. 8a, which are confirmed by the VASP DFT calculations in Fig. 8b (see the details in the ESI†). The amorphous shell of TiO_{2-x} loses lattice periodicity and breaks the octahedral symmetry of TiO_6, and two tails of the VBM and CBM are formed which can narrow the band gap of TiO_2. Furthermore, the oxygen vacancies generated in the shell result in enormous Ti^{3+}, and then the Fermi level of TiO_{2-x} is shifted near CBM.

There are two routes for light excitation in the TiO_{2-x} samples: one arises from the Ti^{3+} $3d^1$ electrons near the Fermi level (close to CBM), and another from the O $2p^6$ electrons near VBM. The black coloration partially results from the transitions (Ti^{3+} $3d^1$ → Ti^{3+} $3d^1$ or Ti^{4+} $3d^0$) of the Ti^{3+} $3d^1$ electrons to the unoccupied Ti 3d states. The light absorption near VBM (O^{2-} $2p^6$ → Ti^{3+} $3d^1$ or Ti^{4+} $3d^0$) is probably more effective for photocatalysis due to the longer life time of light-excited e–h pairs, which was observed by the photoluminescence (PL) measurement (Fig. S17†). From our DFT results and the literature data,[16,39–42] the tail of CBM from Ti^{3+} $3d^1$ is about ~0.7 eV below the CBM of TiO_2 (E_F), and the tail of the VBM from O 2p states is about ~0.4 eV above the VBM of TiO_2 (E_1), which promise the better photoactivity than pristine TiO_2.

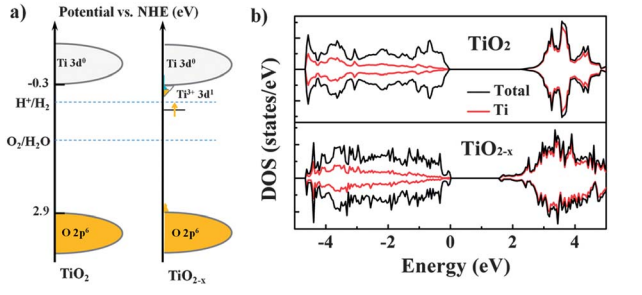

Fig. 8 (a) Schematic electronic structures of TiO_2 and TiO_{2-x}. (b) Total DOS and partial DOS (Ti) of TiO_2 and TiO_{2-x}.

Conclusions

Aluminum reduction is demonstrated to be an excellent approach suitable to produce oxygen-deficient TiO_{2-x} in an evacuated two-zone furnace. The mechanism of aluminum reduction is attributed to sustaining low oxygen partial pressure from melting aluminum and releasing the O from TiO_2. The as-prepared TiO_{2-x} nanocrystals possess a unique core–shell structure of TiO_2@TiO_{2-x}, inducing significant enhancement of visible and near-infrared photoabsorption. The oxygen-deficient shells are well-controlled by reduction conditions and responsible for enhanced wide-spectrum light absorption, photocatalysis, and photoelectrochemical efficiency. Furthermore, the photothermic effect makes black titania be able to "capture" solar energy in solar thermal collectors. This aluminum reduction approach offers potential for the cost-effective and large scale production of black titania. Overall, our black titania with wide solar spectrum absorption possesses significant potential for more efficient hydrogen generation and water cleaning.

Acknowledgements

Z. Wang, C. Yang and T. Lin contributed equally to this work. This work is financially supported by NSF of China (Grant no. 51125006, 91122034, 51121064), 973/863 Programs of China (Grant no. 2011AA050505, 2009CB939900), CAS program (Grant no. KGZD-EW-303, KJCX2-EW-W11), and STC of Shanghai (Grant no. 13JC1405700).

Notes and references

1 M. Gratzel, *Nature*, 2001, **414**, 338.
2 M. R. Hoffmann, S. T. Martin, W. Choi and D. W. Bahnemann, *Chem. Rev.*, 1995, **95**, 69.
3 A. L. Linsebigler, G. Lu and J. T. Yates, *Chem. Rev.*, 1995, **95**, 735.
4 X. Chen and S. S. Mao, *Chem. Rev.*, 2007, **107**, 2891.
5 Z. Zou, J. Ye, K. Sayama and H. Arakawa, *Nature*, 2001, **414**, 625.
6 X. Lü, F. Huang, X. Mou, Y. Wang and F. Xu, *Adv. Mater.*, 2010, **22**, 3719.
7 X. Lü, X. Mou, J. Wu, D. Zhang, L. Zhang, F. Huang, F. Xu and S. Huang, *Adv. Funct. Mater.*, 2010, **20**, 509.
8 R. Asahi, T. Morikawa, T. Ohwaki, K. Aoki and Y. Taga, *Science*, 2001, **293**, 269.
9 J. H. Park, S. Kim and A. J. Bard, *Nano Lett.*, 2005, **6**, 24.
10 J. Wang, D. N. Tafen, J. P. Lewis, Z. Hong, A. Manivannan, M. Zhi, M. Li and N. Wu, *J. Am. Chem. Soc.*, 2009, **131**, 12290.
11 K. Xie, N. Umezawa, N. Zhang, P. Reunchan, Y. Zhang and J. Ye, *Energy Environ. Sci.*, 2011, **4**, 4211.
12 H. Tong, N. Umezawa and J. Ye, *Chem. Commun.*, 2011, **47**, 4219.
13 Z. Yi, J. Ye, N. Kikugawa, T. Kako, S. Ouyang, H. Stuart-Williams, H. Yang, J. Cao, W. Luo, Z. Li, Y. Liu and R. L. Withers, *Nat. Mater.*, 2010, **9**, 559.
14 G. Wang, H. Wang, Y. Ling, Y. Tang, X. Yang, R. C. Fitzmorris, C. Wang, J. Z. Zhang and Y. Li, *Nano Lett.*, 2011, **11**, 3026.

15 X. Chen, L. Liu, P. Y. Yu and S. S. Mao, *Science*, 2011, **331**, 746.
16 H. Pan, Y. W. Zhang, V. B. Shenoy and H. Gao, *J. Phys. Chem. C*, 2011, **115**, 12224.
17 S. Hoang, S. P. Berglund, N. T. Hahn, A. J. Bard and C. B. Mullins, *J. Am. Chem. Soc.*, 2012, **134**, 3659.
18 C. Sun, Y. Jia, X. H. Yang, H. G. Yang, X. Yao, G. Q. Lu, A. Selloni and S. C. Smith, *J. Phys. Chem. C*, 2011, **115**, 25590.
19 X. Jiang, Y. Zhang, J. Jiang, Y. Rong, Y. Wang, Y. Wu and C. Pan, *J. Phys. Chem. C*, 2012, **116**, 22619.
20 A. Naldoni, M. Allieta, S. Santangelo, M. Marelli, F. Fabbri, S. Cappelli, C. L. Bianchi, R. Psaro and V. D. Santo, *J. Am. Chem. Soc.*, 2012, **134**, 7600.
21 Z. Zheng, B. Huang, J. Lu, Z. Wang, X. Qin, X. Zhang, Y. Dai and M. H. Whangbo, *Chem. Commun.*, 2012, **48**, 5733.
22 F. Zuo, K. Bozhilov, R. J. Dillon, L. Wang, P. Smith, X. Zhao, C. Bardeen and P. Feng, *Angew. Chem., Int. Ed.*, 2012, **51**, 6223.
23 X. Lu, G. Wang, T. Zhai, M. Yu, J. Gan, Y. Tong and Y. Li, *Nano Lett.*, 2012, **12**, 1690.
24 J. B. Lu, Y. Dai, H. Jin and B. B. Huang, *Phys. Chem. Chem. Phys.*, 2011, **13**, 18063.
25 X. Chen, L. Liu, Z. Liu, M. A. Marcus, W. Wang, N. A. Oyler, M. E. Grass, B. Mao, P. Glans, P. Y. Yu, J. Guo and S. S. Mao, *Sci. Rep.*, 2013, **3**, 1510.
26 Z. Wang, C. Yang, T. Lin, H. Yin, P. Chen, D. Wan, F. Xu, F. Huang, J. Lin, X. Xie and M. Jiang, *Adv. Funct. Mater.*, 2013, DOI: 10.1002/adfm.201300486.
27 O. Kubaschewski and W. A. Dench, *Acta Metall.*, 1955, **3**, 339.
28 A. L. Bassi, D. Cattaneo, V. Russo, C. E. Bottani, E. Barborini, T. Mazza, P. Piseri, P. Milani, F. O. Ernst, K. Wegner and S. E. Pratsinis, *J. Appl. Phys.*, 2005, **98**, 074305.
29 J. C. Parker and R. W. Siegel, *J. Mater. Res.*, 1990, **5**, 1246.
30 N. H. Hong, A. Barla, J. Sakai and N. Q. Huong, *Phys. Status Solidi C*, 2007, **4**, 4461.
31 Q. Zhao, P. Wu, B. L. Li, Z. M. Lu and E. Y. Jiang, *J. Appl. Phys.*, 2008, **104**, 073911.
32 J. C. Conesa and J. Soria, *J. Phys. Chem.*, 1982, **86**, 1392.
33 J. Pan, G. Liu, G. Q. Lu and H. M. Cheng, *Angew. Chem., Int. Ed.*, 2011, **50**, 2133.
34 R. M. Hochstrasser and S. K. Lower, *J. Chem. Phys.*, 1962, **36**, 3505.
35 J. M. Kuiper and J. B. F. N. Engbert, *Langmuir*, 2004, **20**, 1152.
36 D. L. Beveridge, *J. Am. Chem. Soc.*, 1966, **88**, 1948.
37 X. Chen, S. Shen, L. Guo and S. S. Mao, *Chem. Rev.*, 2010, **110**, 6503.
38 I. S. Cho, Z. Chen, A. J. Forman, D. R. Kim, P. M. Rao, T. F. Jaramillo and X. Zheng, *Nano Lett.*, 2011, **11**, 4978.
39 D. C. Cronemeyer, *Phys. Rev.*, 1959, **113**, 1222.
40 D. C. Cronemeyer and M. A. Gilleo, *Phys. Rev.*, 1951, **82**, 975.
41 I. Justicia, P. Ordejon, G. Canto, J. L. Mozos, J. Fraxedes, G. A. Battiston, R. Gerbasi and A. Figueras, *Adv. Mater.*, 2002, **14**, 1399.
42 F. Zuo, L. Wang, T. Wu, Z. Y. Zhang, D. Borchardt and P. Y. Feng, *J. Am. Chem. Soc.*, 2010, **132**, 11856.

